Research Square

Preprints are preliminary reports that have not undergone peer review.
They should not be considered conclusive, used to inform clinical practice,
or referenced by the media as validated information.

Carbonate-Assisted Structural Stabilization and Physical Properties of Layered Ba3Yb2O5CO3

Koustav Pal Koustav Pal

koustav.pal97@gmail.com

South China University of Technology

Sk Kalimuddin Sk Kalimuddin

Université Paris-Saclay

Behnam Esmaeilzadeh Behnam Esmaeilzadeh

South China University of Technology

I. Das I. Das

Saha Institute of Nuclear Physics

Research Article

Keywords:

Posted Date: November 18th, 2026

DOI: https://doi.org/10.21203/rs.3.rs-11553142/v1

License: This work is licensed under a Creative Commons Attribution 4.0 International License.
Read Full License

Additional Declarations: No competing interests reported.

Carbonate-Assisted Structural Stabilization and Physical Properties of Layered $Ba_3Yb_2O_5CO_3$

Koustav Pal,[1,*] Sk Kalimuddin,[2] Behnam Esmaeilzadeh,[1] and I. Das[3,†]

[1] *South China University of Technology, Guangzhou, Guangdong Province, 511442, China*
[2] *Present address: SPEC, CEA, CNRS, Université Paris-Saclay, CEA Saclay, 91191 Gif-sur-Yvette Cedex, France*
[3] *Retired: Saha Institute of Nuclear Physics, A CI of Homi Bhabha National Institute, Kolkata 700064, India*

(Dated: October 29, 2026)

Polyatomic oxyanion incorporation provides a powerful yet underexplored paradigm to bypass fundamental steric boundaries and synthesize functional architectures beyond the reach of conventional cation engineering. Here, we demonstrate that inserting planar carbonate groups stabilizes the layered triple perovskite $Ba_3Yb_2O_5CO_3$, relieving the severe apical bond mismatch that renders the hypothetical parent oxide "$Ba_3Yb_2O_6$" thermodynamically inaccessible. The symmetry incompatibility between the three-fold (D_{3h}) trigonal unit and the four-fold rotational perovskite cavity induces localized orientational disorder, endowing the rigid inorganic lattice with internal structural adaptability. This oxyanion architecture governs a distinct thermal evolution: elevated-temperature dielectric dispersion dominated by interfacial polarization and localized anion dynamics evolves upon cooling into an intrinsic, low-loss dielectric plateau. Simultaneously, the magnetic response reveals dominant antiferromagnetic exchange correlations and a magnetic moment approaching the free-ion limit, transitioning via single-ion crystalline electric field depopulation toward a well-defined ground state. The concurrence of dielectric stabilization and a magnetic crossover highlights how oxyanion-induced coordination geometry simultaneously influences dielectric response and localized $4f$ spin manifolds. By demonstrating oxyanion insertion as a general mechanism for steric strain relief, these findings provide a predictive roadmap for synthesizing previously inaccessible layered perovskite phases and open versatile design avenues for low-loss cryogenic dielectric ceramics and structurally tailored rare-earth magnetic platforms.

I. INTRODUCTION

Perovskite-structured oxides (ABO_3) and their cation- and anion-ordered derivatives—such as double ($A_2BB'O_6$) and triple ($A_3B_2B'O_9$) perovskites—form a broad class of functional materials in solid-state chemistry and condensed matter physics [1–4]. Accommodation of diverse A- and B-site cations within the corner-sharing BO_6 octahedral network supports phenomena ranging from superconductivity and magnetoresistance to ferroelectricity, multiferroicity, and ionic conduction [3, 5, 6]. Alongside cationic substitution, mixed-anion chemistry—replacing oxide ions (O^{2-}) with halides (F^-, Cl^-), chalcogenides (S^{2-}, Se^{2-}), pnictides (N^{3-}), or polyatomic oxyanions—has been studied for decades as a route to modify coordination environments, anion ordering, metal–ligand covalency, and superexchange pathways in perovskite-related architectures [7–17].

Within the mixed-anion perovskite family, the incorporation of planar carbonate (CO_3^{2-}), nitrate (NO_3^-), or tetrahedral sulfate/phosphate oxyanions stabilizes layered intergrowths that have no pure-oxide counterparts [7, 8, 18–20]. Early work on cuprate oxycarbonates such as $(Ba,Sr)_4Cu_2(CO_3)O_{4+\delta}$ and $Sr_2CuO_2(CO_3)$ established that triangular CO_3^{2-} groups (D_{3h} symmetry in isolation) can replace entire metal–oxygen sheets [18–20]. Because a three-fold planar CO_3^{2-} unit is symmetry-incompatible with the four-fold axis of a tetragonal ($P4/mmm$) perovskite subcell, the carbonate group exhibits four-fold orientational disorder across the basal plane, while coordination of its apical oxygens to adjacent cations distorts the local oxyanion geometry toward C_{2v} symmetry [Figs. 1(b)–(f)] [7, 21].

Deakin *et al.* [21] demonstrated that this carbonate-insertion mechanism stabilizes the layered rare-earth perovskite oxycarbonate series $Ba_3Ln_2O_5CO_3$ (Ln = Y, Dy, Ho, Er, Tm, Yb, Lu) and determined the tetragonal $P4/mmm$ structure of $Ba_3Yb_2O_5CO_3$ ($a = 4.3258(2)$ Å, $c = 11.9036(5)$ Å) using combined X-ray and time-of-flight (TOF) neutron powder diffraction. Structurally, the hypothetical parent oxide "$Ba_3Yb_2O_6$" ($A_3B_2O_6$) is a B-site- and anion-deficient derivative of an $A_3B_3O_9$ triple perovskite ($c \approx 3a_p$), obtained by removing every third BO_2 sheet at $z = 0.5$ together with an oxygen atom so that double $[Ba_2Yb_2O_5]^{2+}$ slabs are separated by a [BaO] plane at $z = 0.5$ [Fig. 1(h)]. Unlike the strontium analogue $Sr_3Ln_2O_6$, "$Ba_3Yb_2O_6$" cannot be synthesized and phase-separates into $Ba_3Yb_4O_9$ and barium oxides [21–23]. As shown by Deakin *et al.* [21], the large twelve-coordinate Ba^{2+} cation ($r_{Ba^{2+}} = 1.61$ Å [24]) expands the c-axis to 11.904–11.915 Å; in hypothetical "$Ba_3Yb_2O_6$," a single monatomic O^{2-} ion fixed at $(0.5, 0.5, 0.5)$ would lie $(0.500 - 0.1773) \times 11.9036$ Å $= 3.841$ Å from the adjacent Yb^{3+} ions at $z = 0.1773$ (or 3.932 Å us-

* koustav.pal97@gmail.com, koustavpal001@scut.edu.cn
† sinp.idas@gmail.com

ing the laboratory XRD coordinate $z = 0.170$ and $c = 11.915$ Å), far exceeding a bonding $Yb^{3+} - O^{2-}$ distance ($\sim$ 2.27 Å). Replacing that single O^{2-} ion at $z = 0.500$ with a vertically oriented CO_3^{2-} group introduces an $O4 - C - O4$ bridge spanning 2.335 Å along c ($z = 0.4019$ and $z = 0.5981$ in the unconstrained neutron refinement of Ref. [21], or 2.526 Å for $z = 0.3940$ and 0.6060 in the initial constrained model), so that two separate oxygen atoms (O4) extend along $\pm c$ to coordinate the lower and upper Yb^{3+} ions at a realistic apical distance of 2.711(11) Å [Fig. 1(g)] [21].

While the synthesis, Raman carbonate stretching modes, and crystal structure of $Ba_3Yb_2O_5CO_3$ were established by Deakin *et al.* [21], its core-level/valence-band photoemission spectra, magnetic susceptibility, and dielectric permittivity have not been previously reported. Here, after verifying phase formation of polycrystalline $Ba_3Yb_2O_5CO_3$ by laboratory powder XRD against the neutron structural model of Ref. [21], we report three characterization datasets: (i) room-temperature X-ray photoelectron spectroscopy (XPS) of the Ba $3d$, C $1s$, Yb $4d$, O $1s$, and valence-band regions; (ii) DC magnetic susceptibility $\chi(T)$ (2–314 K) and room-temperature isothermal magnetization $M(H)$ analyzed via a modified Curie–Weiss model and compared with related Yb^{3+} ($4f^{13}$, $^2F_{7/2}$) oxides and oxyanion compounds such as $Yb_2O_2CO_3$ [25], $Ba_3Yb(BO_3)_3$ [26], $NaYbO_2$ [27], and Yb_2O_3 [28]; and (iii) temperature- and frequency-dependent dielectric permittivity $\varepsilon'(T, f)$ and loss tangent $\tan\delta(T, f)$ scans (15–300 K, 107 Hz to 1 MHz) on sintered polycrystalline pellets, which separate the low-temperature permittivity plateau below 150 K from the high-temperature Maxwell–Wagner interfacial step [29–32]. We also explicitly discuss the experimental limitations of these measurements, including surface carbonate overlap in unetched XPS, parameter covariance and crystal-electric-field (CEF) effects in high-temperature Curie–Weiss fits, and electrode/leakage artifacts in high-temperature polycrystalline dielectric scans.

II. EXPERIMENTAL DETAILS

Polycrystalline $Ba_3Yb_2O_5CO_3$ was prepared by solid-state reaction of stoichiometric $BaCO_3$ and Yb_2O_3 (3 : 1 molar ratio) ground in an agate mortar for 2 h ($3\,BaCO_3 + Yb_2O_3 \rightarrow Ba_3Yb_2O_5CO_3 + 2\,CO_2\uparrow$) [21]. Loose precursor powders in an alumina boat were calcined for 12 h in a tube furnace under a continuous flow of dry N_2 gas (nominal heating and cooling rates of $5\,^\circ C \cdot min^{-1}$, unmonitored N_2 flow rate). In our furnace setup, a nominal setpoint of 950 °C yielded $Ba_3Yb_2O_5CO_3$ with a minor unreacted Yb_2O_3 secondary phase, whereas a 900 °C setpoint left unreacted $BaCO_3$ and Yb_2O_3, and a 965 °C setpoint produced decomposition into $Ba_3Yb_4O_9$ [22, 23]. For dielectric measurements, the 950 °C-calcined powder was uniaxially cold-pressed into a cylindrical pellet and re-sintered at the same nominal setpoint of 950 °C for 12 h under flowing dry N_2. Room-temperature powder XRD on a pulverized portion of the sintered pellet confirmed retention of the $P4/mmm$ phase without decomposition into $Ba_3Yb_4O_9$; however, geometric/Archimedes bulk density, porosity, and scanning electron microscopy (SEM) microstructure of the sintered compact were not measured, and independent vibrational or thermal carbonate analyses (FTIR, Raman, or TGA-MS) were not performed in this study (bulk carbonate incorporation in $Ba_3Yb_2O_5CO_3$ synthesized by this route was previously confirmed via the ν_1 symmetric carbonate Raman stretch at 1054.51 cm^{-1} by Deakin *et al.* [21]).

Room-temperature powder X-ray diffraction (XRD) was collected on a Rigaku SmartLab diffractometer (Cu K_α radiation, $\lambda = 1.5406$ Å) over $2\theta = 10°$–$90°$. Single-phase Rietveld refinement of the main $P4/mmm$ phase was performed in FullProf [33] starting from the neutron structural model of Deakin *et al.* [21], and crystal structures were drawn with VESTA [34].

Room-temperature X-ray photoelectron spectroscopy (XPS) of the O $1s$, Ba $3d$, C $1s$, Yb $4d$, and valence-band regions was carried out on an air-exposed pellet surface (without *in situ* Ar^+ sputtering or vacuum fracturing) using an OMICRON spectrometer equipped with a SCIENTA OMICRON SPHERA hemispherical analyzer and a monochromatic Al K_α source ($h\nu = 1486.6$ eV). No electron flood gun (charge neutralizer) was used during acquisition. Peak fitting with Gaussian–Lorentzian profiles and Shirley backgrounds was performed in KolXPD [35]. On the as-acquired spectrometer binding-energy scale (referenced to the instrumental Fermi level, $E_F = 0$ eV, as plotted in Figs. 2 and 3), the adventitious hydrocarbon ($C - C/C - H$) C $1s$ peak lies at 283.74 eV; both the as-measured binding energies and the values shifted by +1.06 eV to place adventitious C $1s$ at 284.80 eV are listed in Table III, alongside known caveats regarding adventitious carbon referencing on insulating oxides [36, 37].

Direct-current (DC) magnetic susceptibility $\chi(T) = M/H$ was measured from 2 K to 314 K under applied magnetic fields of $H = 500$ Oe and 1000 Oe under zero-field-cooled (ZFC) and field-cooled (FC) conditions, and isothermal magnetization $M(H)$ was measured at $T = 300$ K up to ±50 kOe (±5 T) in a Quantum Design SQUID-VSM magnetometer. Temperature-dependent dielectric measurements were performed in a two-probe parallel-plate geometry prepared by applying conductive silver paint to both faces of the sintered pellet. Capacitance and loss factor ($\tan\delta$) were recorded on an LCR meter at discrete off-integer frequencies between 107 Hz and 1 000 007 Hz ($\sim$ 1 MHz, chosen to avoid 50 Hz power-line harmonics) from 15 K to 300 K during cooling and heating sweeps.

III. RESULTS AND DISCUSSION

A. Phase Verification and Structural Context

In our furnace setup under flowing N_2 (12 h dwell), calcination of loose 3 $BaCO_3$: 1 Yb_2O_3 powder at a nominal setpoint of 900 °C left unreacted orthorhombic witherite $BaCO_3$ (ICDD PDF No. 01-071-6423) [38] and cubic C-type Yb_2O_3 [23], whereas firing at 950 °C yielded the tetragonal $Ba_3Yb_2O_5CO_3$ phase [Fig. 1(a)] with weak unindexed reflections near $2\theta \approx 35°$ and 50° attributable to minor residual Yb_2O_3 (estimated visually at $< 2\%$ intensity, as Yb_2O_3 was not included as a second phase in the refinement; compare the 2.5 wt% Yb_2O_3 residual reported in the neutron refinement of Ref. [21]). Heating the loose powder bed to a nominal setpoint of 965 °C resulted in decomposition into $Ba_3Yb_4O_9$ [22, 23]. By comparison, Deakin *et al.* [21] reported that $Ba_3Ln_2O_5CO_3$ phases form via solid-state reaction at $\leq$ 1000 °C in air (as well as at 950–1050 °C under dry N_2 with intermittent regrinding) and decompose into $Ba_3Ln_4O_9$ above 1000 °C in air. Because a 15 °C nominal setpoint difference (950 °C vs. 965 °C) lies within typical tube-furnace temperature gradients and because carrier-gas flow rate, sample bed depth, and local CO_2 partial pressure were not systematically controlled or monitored by thermogravimetric analysis (TGA-MS), the lower decomposition setpoint observed here reflects the specific kinetics and low local CO_2 partial pressure of our open-boat N_2-sweep configuration rather than an intrinsic thermodynamic boundary.

Profile refinement of our room-temperature laboratory XRD pattern [Fig. 1(a)] confirms that the sample adopts the tetragonal $P4/mmm$ structure with unit cell parameters $a = b = 4.326(1)$ Å, $c = 11.915(3)$ Å, and $V = 222.98(7)$ Å^3, closely matching the neutron diffraction values reported by Deakin *et al.* [21] ($a = 4.3258(2)$ Å, $c = 11.9036(5)$ Å, $V = 222.75(2)$ Å^3). As shown in Table I, because X-ray scattering factors scale with atomic number Z, heavy Yb ($Z = 70$) and Ba ($Z = 56$) dominate the laboratory XRD intensities, rendering X-ray diffraction insensitive to the light C ($Z = 6$) and O ($Z = 8$) positions and site occupancies. Specifically, allowing the equatorial oxygen coordinate z_{O1} to vary in an unconstrained laboratory XRD refinement shifts z_{O1} to 0.235 compared with the neutron-refined value of 0.1995(3) [21]—a discrepancy of $\Delta z \times c \approx 0.42$ Å that artificially distorts the apparent XRD Yb − O1 (2.297 Å) and Yb − O2 (2.026 Å) bond lengths relative to the true neutron values [d(Yb1 − O1) = 2.179(1) Å and d(Yb1 − O2) = 2.110(3) Å]. Likewise, unconstrained XRD refinements of the fractional occupancies of O3 (0.21) and O4 (0.27) have negligible leverage on the X-ray fit quality. We also note that global profile residuals (R_{wp}, R_p, χ^2) and a two-phase quantitative refinement of the minor Yb_2O_3 fraction were not archived from the FullProf session. Consequently, our laboratory XRD pattern serves strictly to confirm phase formation and unit-cell dimensions, while all interatomic distances and angles in Table II and in the discussion below are taken from the benchmark TOF neutron diffraction structure of Deakin *et al.* [21].

In the neutron structure of $Ba_3Yb_2O_5CO_3$ [21], double perovskite slabs $[Ba_2Yb_2O_5]^{2+}$ alternate along c with $[Ba(CO_3)]^{2-}$ layers at $z = 0.5$ [Fig. 1(b)]. Within each $[Ba_2Yb_2O_5]^{2+}$ slab, two YbO_5 square pyramids share a common apical oxygen O2 at $(0.5, 0.5, 0)$, giving a short intra-slab apical bond d(Yb1 − O2) = 2.110(3) Å (an intra-bilayer Yb ⋯ Yb distance of 4.221 Å along c) and four equatorial bonds d(Yb1 − O1) = 2.179(1) Å (an in-plane Yb ⋯ Yb distance of $a = 4.326$ Å). The large O1 ($U_{33} = 0.071(1)$ Å^2) and O2 ($U_{11} = U_{22} = 0.088(1)$ Å^2) anisotropic displacement components revealed by neutron diffraction indicate static or dynamic local tilting of the YbO_6 polyhedra coupled to the local orientation of the adjacent carbonate group [21]. Across the $z = 0.5$ mirror plane, the two Yb^{3+} ions at $z_{Yb} = 0.1773$ and $1 - z_{Yb} = 0.8227$ are separated by $(1 - 2z_{Yb})c = 7.683$ Å. In hypothetical "$Ba_3Yb_2O_6$" [Fig. 1(h)], a single O^{2-} ion at $(0.5, 0.5, 0.5)$ would lie at a non-bonding distance of:

$$d(\mathrm{Yb} - \mathrm{O})_{\mathrm{hyp}} = (0.500 - 0.1773)\, c = 3.841 \text{ Å} \qquad (1)$$

(or 3.932 Å for $z_{Yb} = 0.170$ and $c = 11.915$ Å). In $Ba_3Yb_2O_5CO_3$ [Fig. 1(g)], the vertically oriented CO_3^{2-} group places its carbon atom at C1$(0.5, 0.435, 0.5)$ and its in-plane oxygen at O3$(0.5, 0.148, 0.5)$ [d(C1 − O3) = 1.242(16) Å], while its two out-of-plane oxygens occupy the 8t split sites at $z = 0.4019(9)$ and $1 - z = 0.5981(9)$ [d(C1 − O4) = 1.376(10) Å in the $x = 0.5$ mirror plane] [21]. As summarized in Table II, within the $x = 0.5$ carbonate plane, the two ∠O3 − C1 − O4 angles of 121.9° and one ∠O4 − C1 − O4 angle of 116.2° sum to 360.0° (close to the ideal 120° trigonal planar geometry), while projecting O4 to within 2.711(11) Å of the adjacent Yb^{3+} cations to complete an elongated [5 + 1] YbO_6 coordination polyhedron [21].

B. X-ray Photoelectron Spectroscopy

Room-temperature XPS spectra of the Ba 3d, C 1s, Yb 4d, and O 1s core levels are shown in Figs. 2(a)–2(d), and the valence-band spectrum is shown in Fig. 3. Because the spectra were collected without an electron flood gun on an insulating pellet, the as-measured binding energies (plotted on the horizontal axes of Figs. 2 and 3) place the adventitious hydrocarbon (C − C/C − H) C 1s peak at 283.74 eV. Table III lists both the as-measured peak positions and the values shifted by +1.06 eV to align adventitious C 1s to the conventional 284.80 eV reference, noting that adventitious carbon referencing on insulating oxides is subject to work-function and differential-charging uncertainties of several tenths of an eV [36, 37], whereas relative peak separations (ΔE_B and Δ_{SO}) within a given core-level window are insensitive to uniform charging shifts.

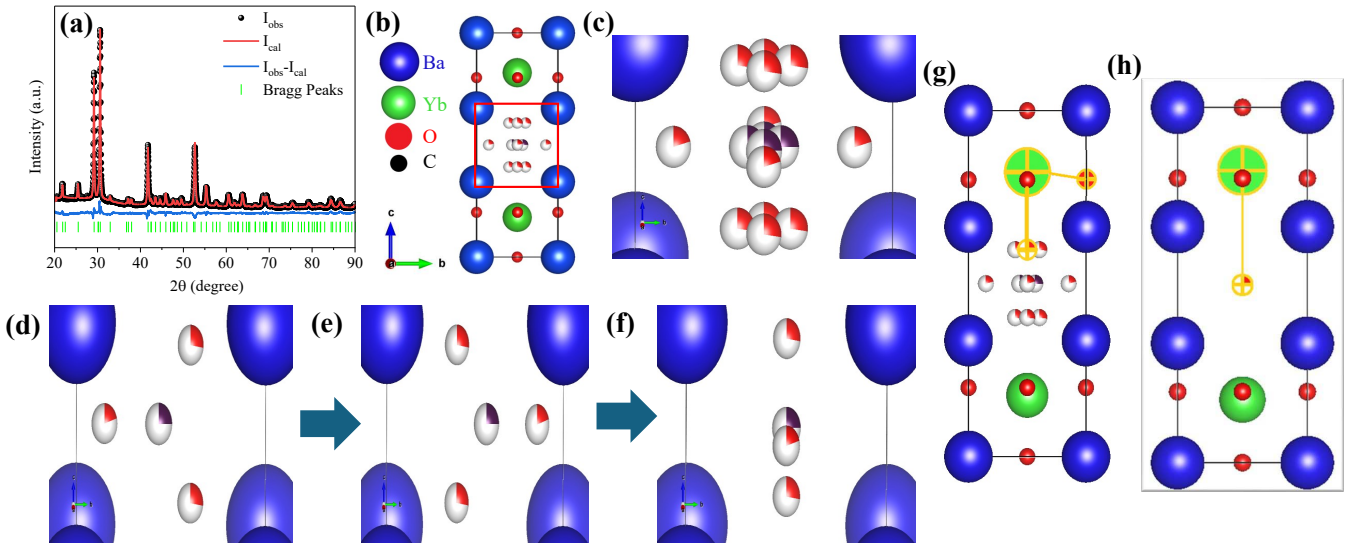


FIG. 1. (a) Room-temperature powder XRD pattern and Rietveld profile of $Ba_3Yb_2O_5CO_3$ refined in tetragonal space group $P4/mmm$ ($a = 4.326(1)$ Å, $c = 11.915(3)$ Å). Experimental data (I_{obs}, open black circles), calculated pattern (I_{cal}, solid red line), difference curve ($I_{obs} - I_{cal}$, lower blue line), and $Ba_3Yb_2O_5CO_3$ Bragg reflection positions (vertical green tick marks) are shown; weak unindexed peaks near $2\theta \approx 35°$ and 50° correspond to minor unreacted Yb_2O_3. (b) Crystal structure of $Ba_3Yb_2O_5CO_3$ viewed along the a-axis (b–c plane), showing double $[Ba_2Yb_2O_5]^{2+}$ slabs separated by a $[Ba(CO_3)]^{2-}$ layer at $z = 0.5$ [21]. (c) View of the central oxyanion plane at $z = 0.5$, where sector-shaded spheres depict the four-fold disordered C ($4o$), in-plane O3 ($4o$), and out-of-plane O4 ($8t$) split sites. (d)–(f) Schematic representations of two individual local orientations of the planar CO_3^{2-} unit [(d) and (e)] and their four-fold statistical superposition [(f)] in the tetragonal cavity [21]. (g) Coordination polyhedra in $Ba_3Yb_2O_5CO_3$, where the vertically oriented CO_3^{2-} group projects two out-of-plane O4 atoms along $\pm c$ ($z = 0.4019$ and $z = 0.5981$, spanning 2.335 Å in the unconstrained neutron refinement of Ref. [21], or $z = 0.3940$ and 0.6060 spanning 2.526 Å in the constrained model), yielding an apical Yb − O4 bond length of 2.711(11) Å [21]. (h) Hypothetical oxide "$Ba_3Yb_2O_6$" ($A_3B_2O_6$), showing the unphysically long apical separation from Yb^{3+} to a single isolated O^{2-} ion at $(0.5, 0.5, 0.5)$ [3.841 Å using the neutron parameters $z_{Yb} = 0.1773$ and $c = 11.9036$ Å of Ref. [21], or 3.932 Å using the XRD coordinate $z_{Yb} = 0.170$ and $c = 11.915$ Å]. Crystal structures were drawn with VESTA [34].

The Ba $3d$ spectrum [Fig. 2(a)] consists of the Ba $3d_{5/2}$ and Ba $3d_{3/2}$ peaks at 778.78 eV and 794.09 eV as-measured (779.84 eV and 795.15 eV referenced to C $1s$ = 284.80 eV), separated by a spin–orbit splitting of:

$$\Delta_{SO}(\mathrm{Ba}\,3d) = E_B(\mathrm{Ba}\,3d_{3/2}) - E_B(\mathrm{Ba}\,3d_{5/2}) = 15.31\ \mathrm{eV}, \quad (2)$$

consistent with divalent Ba^{2+} [39]. In the C $1s$ region [Fig. 2(b)], a higher-binding-energy component appears at $\Delta E_B = +4.16$ eV above the adventitious hydrocarbon peak (287.90 eV as-measured; 288.96 eV referenced), characteristic of carbon in a carbonate (CO_3^{2-}) environment [39]. Similarly, the O $1s$ envelope [Fig. 2(d)] is fitted by two components separated by $\Delta E_B = +0.81$ eV, located at 529.94 eV and 530.74 eV as-measured (531.00 eV and 531.80 eV referenced).

An important experimental caveat must be emphasized regarding the Ba $3d$, C $1s$, and O $1s$ core levels. Because XPS probes only the top ∼ 2–5 nm of an air-exposed pellet and alkaline-earth oxides readily react with ambient CO_2 and H_2O, surface $BaCO_3$ and $Ba(OH)_2$ species commonly form on barium-containing perovskites. Reference XPS spectra of bulk $BaCO_3$ exhibit Ba $3d_{5/2} \approx 779.6$–780.0 eV, C $1s \approx 289.0$–289.3 eV, and O $1s \approx 531.2$–531.6 eV [39], which closely overlap the charge-referenced binding energies in Table III. In the absence of *in situ* vacuum fracturing, Ar^+ depth profiling, a co-measured $BaCO_3$ reference standard, or bulk vibrational spectroscopy (FTIR/Raman) on the same pellet, XPS alone cannot distinguish bulk structural CO_3^{2-} groups from superficial $BaCO_3$/hydroxide layers.

In the Yb $4d$ core-level region [Fig. 2(c)], photoemission from trivalent Yb^{3+} ($4f^{13}$) produces a $4d^9 4f^{13}$ two-hole final-state configuration in which strong $4d$–$4f$ Coulomb and exchange interactions comparable to the $4d$ spin–orbit coupling split the spectrum into a broad, multi-peak multiplet manifold (^{1}P,^{3} H,^{3} G,^{3} F,… final states spanning 182–205 eV) rather than a simple single-particle $4d_{5/2}$–$4d_{3/2}$ doublet [40–43]. The three-peak Gaussian–Lorentzian decomposition shown in Fig. 2(c) (with maxima at 184.30, 188.50, and 190.95 eV as-measured, or 185.36, 189.56, and 192.01 eV referenced; labeled as "Yb $4d_{5/2}$," "Yb − O peaks," and "Yb $4d_{3/2}$" in the raw fitting plot) is therefore an empirical parameterization of the three principal intensity envelopes of the Yb^{3+} $4d^9 4f^{13}$ multiplet profile reported for Yb_2O_3 [42, 43]. Within the signal-to-noise ratio of Fig. 2(c), no sharp lower-binding-energy $4d^9 4f^{14}$ spin–orbit doublet charac-

TABLE I. Crystallographic Wyckoff sites, fractional coordinates, site occupancies, and isotropic or equivalent isotropic displacement parameters (U_{iso}/U_{eq}) for $Ba_3Yb_2O_5CO_3$ in tetragonal space group $P4/mmm$ (No. 123, $Z = 1$), comparing the present room-temperature laboratory powder XRD profile refinement ($a = b = 4.326(1)$ Å, $c = 11.915(3)$ Å, $V = 222.98(7)$ Å^3) with the benchmark time-of-flight (TOF) powder neutron diffraction structure of Deakin *et al.* [21] ($a = 4.3258(2)$ Å, $c = 11.9036(5)$ Å, $V = 222.75(2)$ Å^3, $R_{wp} = 2.93\%$, GOF = 1.71). Because X-ray scattering is dominated by heavy Yb ($Z = 70$) and Ba ($Z = 56$), light-atom (C, O) coordinates and occupancies are not reliably constrained by laboratory XRD (for example, unconstrained XRD gives $z_{O1} = 0.235$ vs. the true neutron value 0.1995(3), a ~ 0.42 Å shift along c); therefore, all structural analysis relies on the neutron coordinates of Ref. [21].

Atom	Wyckoff Site	x	y	z (XRD)	z (Neutron [21])	Occupancy (XRD / Neutron [21])	U_{iso} or U_{eq} (Å^2, Ref. [21])
Ba1	1*a*	0	0	0	0	1.00 / 1.000	0.028(1)[a]
Ba2	2*g*	0	0	0.328(1)	0.3358(6)	1.00 / 1.000	0.026(1)[a]
Yb1	2*h*	0.5	0.5	0.170(1)	0.1773(2)	1.00 / 1.000	0.018(1)
O1	4*i*	0	0.5	0.235[b]	0.1995(3)	1.00 / 1.000	0.035(1)[a]
O2	1*c*	0.5	0.5	0	0	1.00 / 1.000	0.060(1)[a]
C1	4*o*	0.5	0.435(2)[c]	0.5	0.5	0.25 / 0.250	0.009(1)
O3	4*o*	0.5	0.148(3)[c]	0.5	0.5	0.21[b] / 0.210(14)[d]	0.016(3)[a]
O4	8*t*	0.397(2)[c]	0.5	0.394[c]	0.4019(9)	0.27[b] / 0.270(7)[d]	0.049(2)[a]

[a]Equivalent isotropic displacement parameter $U_{eq} = \frac{1}{3}(U_{11} + U_{22} + U_{33})$ calculated from the anisotropic thermal parameters refined by TOF neutron diffraction in Table 1 of Ref. [21]: Ba1 ($U_{11} = U_{22} = 0.034(1)$, $U_{33} = 0.015(3)$ Å^2), Ba2 ($U_{11} = U_{22} = 0.024(1)$, $U_{33} = 0.030(2)$ Å^2), O1 ($U_{11} = 0.008(1)$, $U_{22} = 0.026(1)$, $U_{33} = 0.071(1)$ Å^2), O2 ($U_{11} = U_{22} = 0.088(1)$, $U_{33} = 0.004(2)$ Å^2), O3 ($U_{11} = U_{22} = 0.020(5)$, $U_{33} = 0.008(5)$ Å^2), and O4 ($U_{11} = 0.043(2)$, $U_{22} = U_{33} = 0.052(2)$, $U_{13} = -0.013(1)$ Å^2).

[b]Unconstrained laboratory XRD values for light oxygen sites (O1 z-coordinate and O3/O4 occupancies) suffer from severe form-factor insensitivity in the presence of heavy Ba and Yb and are shown only to illustrate the limitation of X-ray refinement.

[c]In the laboratory XRD profile fit, the carbonate coordinates were fixed to the initial constrained model ($x_{O4} = 0.390$, $z_{O4} = 0.3940$), whereas the unconstrained TOF neutron refinement of Deakin *et al.* [21] gave $x_{O4} = 0.397(2)$ and $z_{O4} = 0.4019(9)$.

[d]In Ref. [21], the sum of the carbonate oxygen occupancies was constrained to equal 3 per formula unit ($4 \times 0.210 + 8 \times 0.270 = 3.00$), with ideal stoichiometric values of 0.25 for both O3 (4*o*) and O4 (8*t*).

teristic of divalent Yb^{2+} (expected near 180–182 eV) is resolved, consistent with predominantly trivalent Yb^{3+} (including the minor $< 2\%$ Yb_2O_3 phase).

The room-temperature valence-band photoemission spectrum (Fig. 3) shows negligible spectral intensity at $E_F = 0$ eV, with the leading valence-band edge emerging at $\sim$ 2.5–3.0 eV below E_F (or $\sim$ 3.5–4.0 eV after the +1.06 eV charging shift) and a broad O 2*p* / Yb 4*f* band centered near 7 eV. While this valence-band onset is consistent with electrically insulating behavior, optical diffuse reflectance (UV–vis) measurements would be required to determine the quantitative optical bandgap.

C. Magnetic Susceptibility and Curie–Weiss Analysis

Figure 4(a) displays the molar magnetic susceptibility $\chi(T)$ (normalized per mole of $Ba_3Yb_2O_5CO_3$ formula unit) measured under applied fields of $H = 500$ Oe and 1000 Oe between 2 K and 314 K. The susceptibility increases monotonically upon cooling down to 2 K with no ZFC–FC divergence and no cusp indicative of long-range magnetic ordering. At $T = 300$ K, the isothermal magnetization $M(H)$ [Fig. 4(b)] is strictly linear and anhysteretic up to ± 50 kOe, confirming bulk paramagnetism at room temperature.

Over the high-temperature interval 150–314 K, $\chi(T)$ was fitted to the three-parameter modified Curie–Weiss expression [28]:

$$\chi(T) = \chi_0 + \frac{C_{f.u.}}{T - \theta_{CW}}, \tag{3}$$

where χ_0 is a temperature-independent susceptibility term, $C_{f.u.}$ is the molar Curie constant per formula unit (containing two Yb^{3+} ions), and θ_{CW} is the Weiss temperature. Nonlinear least-squares fitting over 150–314 K [inset of Fig. 4(a)] gives:

$$\chi_0 = 2.66(8) \times 10^{-3}\ \text{emu} \cdot \text{mol}_{f.u.}^{-1} \cdot \text{Oe}^{-1}, \tag{4}$$

$$\theta_{CW} = -60.8(1.5)\ \text{K}, \quad C_{f.u.} = 4.89(6)\ \text{emu} \cdot \text{K} \cdot \text{mol}_{f.u.}^{-1}. \tag{5}$$

From $C_{f.u.} = 4.893\ \text{emu} \cdot \text{K} \cdot \text{mol}_{f.u.}^{-1}$, the effective moment per formula unit is $\mu_{eff,f.u.} = \sqrt{8 C_{f.u.}} = 6.256\,\mu_B$/f.u. Because each formula unit contains two equivalent Yb^{3+} ions ($C_{Yb} = C_{f.u.}/2 = 2.447\ \text{emu} \cdot \text{K} \cdot \text{mol}_{Yb}^{-1}$), the effective magnetic moment per Yb^{3+} ion is obtained by quadrature addition ($\mu_{eff,f.u.}^2 = 2\,\mu_{eff,Yb}^2$, rather than linear division $\mu_{eff,f.u.}/2 = 3.128\,\mu_B$ as printed inside the plot panel of Fig. 4(a)) [28]:

$$\mu_{eff,Yb} = \sqrt{8\,C_{Yb}} = \frac{\mu_{eff,f.u.}}{\sqrt{2}} = 4.42(3)\ \mu_B/\text{Yb}^{3+}. \tag{6}$$

This value is close to the Hund's-rule free-ion effective moment for Yb^{3+} ($4f^{13}$, $^2F_{7/2}$, $S = 1/2$, $L = 3$, $J = 7/2$,

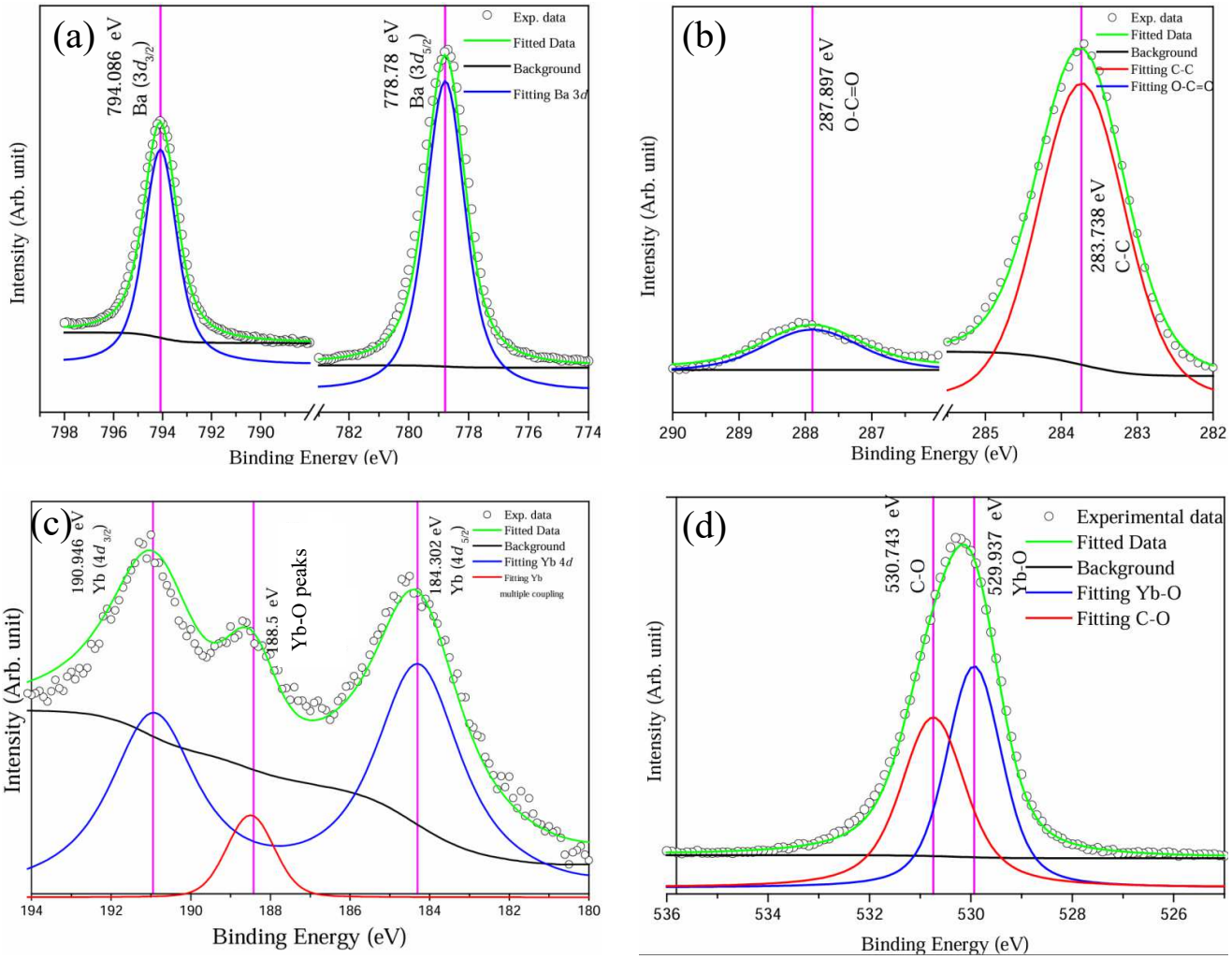


FIG. 2. Room-temperature core-level XPS spectra of $Ba_3Yb_2O_5CO_3$ plotted on the as-measured spectrometer binding-energy scale: (a) Ba $3d$ spin–orbit doublet ($3d_{5/2}$ and $3d_{3/2}$); (b) C $1s$ region fitted with adventitious hydrocarbon (C − C) and carbonate (O − C = O) peaks; (c) Yb $4d$ region showing an empirical three-peak envelope decomposition of the open-shell Yb^{3+} ($4d^9 4f^{13}$) multiplet manifold (note that the single-particle "Yb $4d_{5/2}$," "Yb − O peaks," and "Yb $4d_{3/2}$" annotations inside panel (c) are legacy plotting labels from KolXPD and correspond to the lower, intermediate, and upper $4d^9 4f^{13}$ multiplet envelopes in Table III); and (d) O $1s$ region fitted with lower-binding-energy (Yb − O/oxide) and higher-binding-energy (C − O/carbonate) components. Open circles denote experimental data, black solid lines indicate Shirley backgrounds, blue and red curves show fitted subpeaks, and green solid lines show cumulative envelope fits.

$g_J = 8/7$):

$$\mu_{\text{free}} = g_J \sqrt{J(J+1)}\,\mu_{\text{B}} = \frac{8}{7}\sqrt{\frac{7}{2}\left(\frac{9}{2}\right)}\,\mu_{\text{B}} = 4.54\ \mu_{\text{B}}. \tag{7}$$

Several important limitations and physical considerations apply to the interpretation of the Curie–Weiss fit in Eqs. (3)–(5) and the low-temperature susceptibility behavior:

1. *Parameter Covariance and Magnitude of χ_0:* At $T = 300$ K, the total measured molar susceptibility is $\chi(300\ \text{K}) \approx 1.62 \times 10^{-2}$ emu $\cdot$ mol$_{\text{f.u.}}^{-1} \cdot$ Oe^{-1}, meaning that the fitted constant term $\chi_0 = 2.66 \times 10^{-3}$ emu $\cdot$ mol$_{\text{f.u.}}^{-1} \cdot$ Oe^{-1} constitutes $\sim$ 16–20% of the high-temperature signal. Over the restricted 150–314 K fitting window, χ_0, $C_{\text{f.u.}}$, and θ_{CW} exhibit strong numerical covariance. While a positive χ_0 of order 10^{-3} emu $\cdot$ mol$_{\text{Yb}}^{-1}$ is qualitatively consistent with a second-order Van Vleck contribution from magnetic-field mixing across crystal-electric-field (CEF) levels (potentially combined with sample-holder background) [28, 46], no independent microscopic calculation of the Van Vleck susceptibility has been performed here.

2. *Qualitative Role of CEF Splitting vs. Exchange in θ_{CW}:* As shown for Yb_2O_3 by Mugiraneza and

TABLE II. Selected interatomic bond distances (Å) and carbonate angles (°) in $Ba_3Yb_2O_5CO_3$ from the benchmark powder neutron diffraction structure of Deakin *et al.* [21] (Table 2 of Ref. [21]), together with the planar carbonate angles in the $x = 0.5$ mirror plane and the hypothetical apical distance in "$Ba_3Yb_2O_6$."

Bond / Angle Parameter	Value (Ref. [21])
Yb1 − O1 (equatorial, ×4)	2.179(1) Å
Yb1 − O2 (intra-slab, ×1)	2.110(3) Å
Yb1 − O4 (apical CO_3, ×1)	2.711(11) Å
Ba1 − O1 (×8)	3.212(2) Å
Ba1 − O2 (×4)	3.059(0) Å
Ba2 − O1 (×4)	2.704(5) Å
Ba2 − O3 (×2)[a]	2.985(5) Å
Ba2 − O4 (×4)[a]	2.871(7) Å
C1 − O3 (in-plane, ×1)	1.242(16) Å
C1 − O4 (out-of-plane, ×2)	1.376(10) Å
∠O3 − C1 − O4 (×2)[b]	121.9° (101.8°)
∠O4 − C1 − O4 (×1)[b]	116.2° (156.5°)
Planar carbonate angle sum	360.0°
Apical Yb − O in "$Ba_3Yb_2O_6$"	3.841 Å[c]
Cu − O_{ap} in $Sr_2CuO_2(CO_3)$ [19]	2.730 Å

[a]Local Ba2 − O3 and Ba2 − O4 distances depend on the local orientation of the disordered carbonate group [21].
[b]In the $x = 0.5$ mirror plane containing C1(0.5, 0.435, 0.5), O3(0.5, 0.148, 0.5), and the symmetry-equivalent O4(0.5, 0.603, 0.4019/0.5981) sites corresponding to d(C1 − O4) = 1.376(10) Å in Table 2 of Ref. [21], the carbonate bond angles are 121.9° (×2) and 116.2° (×1). Pairing C1(0.5, 0.435, 0.5) instead with the asymmetric-unit O4(0.397, 0.5, 0.4019) site (or with the constrained coordinates $x_{O4} = 0.390$, $z_{O4} = 0.394$) yields apparent split-site angles of 102.7° and 154.6° (or 101.8° and 156.5° in parenthesis) due to positional averaging across the four disordered orientations.
[c]Calculated from the neutron parameters $z_{Yb} = 0.1773$ and $c = 11.9036$ Å of Ref. [21] [Eq. (1)]; using the XRD coordinate $z_{Yb} = 0.170$ and $c = 11.915$ Å gives $(0.500 - 0.170) \times 11.915 = 3.932$ Å.

Hallas [28] and for related Yb^{3+} oxyanion systems such as $Yb_2O_2CO_3$ [25] and $Ba_3Yb(BO_3)_3$ [26] (Table IV), a large negative high-temperature Weiss intercept ($\theta_{CW}^{HT} \approx -60$ to -95 K) is a generic feature of Yb^{3+} ($4f^{13}$, $^2F_{7/2}$) oxides and does not measure the inter-site exchange interaction. In the non-cubic [5 + 1] YbO_6 coordination environment, the eight-fold degenerate $^2F_{7/2}$ multiplet splits into four Kramers doublets [44, 47–49]. Thermal repopulation of excited CEF doublets over 150–314 K causes the effective moment to increase with temperature toward the 4.54 μ_B free-ion limit, generating a large negative θ_{CW}^{HT} intercept in $\chi^{-1}(T)$ and upward curvature in $1/(\chi - \chi_0)$ below 150 K as excited doublets depopulate [28]. However, without inelastic neutron scattering (INS), Raman spectroscopy, or a multi-level CEF fit, the specific CEF splitting energies in $Ba_3Yb_2O_5CO_3$ remain undetermined.

3. *Intra-Bilayer Pathways and Low-Temperature ($T \leq$ 2 K) Cutoff:* Although the inter-bilayer distance across the $[Ba(CO_3)]^{2-}$ spacer is large (7.68 Å), the Yb^{3+} ions within each $[Ba_2Yb_2O_5]^{2+}$ double-perovskite slab are separated by only 4.221 Å across the linear Yb1 − O2 − Yb1 bridge [d(Yb1 − O2) = 2.110(3) Å] and 4.326 Å across the equatorial Yb1 − O1 − Yb1 pathways [d(Yb1 − O1) = 2.179(1) Å] [21]. Thus, intra-bilayer superexchange pathways are crystallographically short [50], and the absence of magnetic ordering down to 2 K simply reflects the weak $4f$–$2p$ hybridization typical of Yb^{3+} oxides, where exchange constants and ordering temperatures typically lie below 1–2 K (Table IV) [25–27]. Because our susceptibility measurements terminate at 2 K—immediately adjacent to the $T_N = 2.3$ K antiferromagnetic transition of the minor Yb_2O_3 impurity [28]—and because low-temperature isothermal magnetization $M(H)$ and specific heat $C_p(T)$ ($R \ln 2$ magnetic entropy) were not measured, the properties of the lowest Kramers doublet ($J_{eff} = 1/2$) and the intrinsic low-temperature exchange scale (θ_{CW}^{LT}) remain to be determined by sub-kelvin experiments.

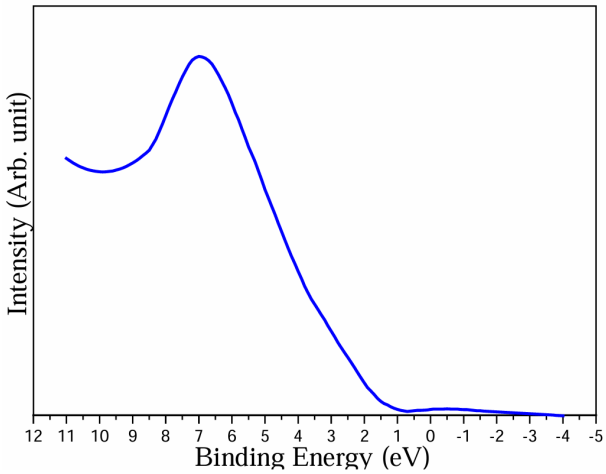


FIG. 3. Room-temperature XPS valence-band spectrum of $Ba_3Yb_2O_5CO_3$ plotted on the as-measured binding-energy scale (−5 eV to +12 eV relative to the instrumental Fermi level $E_F = 0$ eV).

D. Temperature- and Frequency-Dependent Dielectric Permittivity

Figures 5(a) and 5(b) show the temperature dependence of the real dielectric permittivity (ε') of a silver-painted sintered pellet of $Ba_3Yb_2O_5CO_3$ measured from 15 K to 300 K at frequencies between 107 Hz and 1 MHz during cooling and heating sweeps, respectively; the corresponding loss tangent curves ($\tan\delta$) are plotted in Figs. 5(c) and 5(d).

The dielectric scans display two temperature regimes:

TABLE III. Fitted core-level XPS peak positions (both as-measured values matching Fig. 2 and values shifted by +1.06 eV to reference adventitious C 1*s* at 284.80 eV), spin–orbit or subpeak separations (Δ_{SO} / ΔE_B), and nominal assignments for $Ba_3Yb_2O_5CO_3$ (±0.1 eV experimental uncertainty).

Core Level	E_B As-Measured (eV)	E_B Referenced to C 1*s* = 284.80 eV	Δ_{SO} or ΔE_B (eV)	Nominal Assignment
O 1*s*	529.94	531.00	—	Lattice oxide / surface species
	530.74	531.80	$\Delta E_B = +0.81$	Carbonate / surface $-CO_3$ or $-OH$
Ba 3*d*	778.78 ($3d_{5/2}$)	779.84	$\Delta_{SO} = 15.31$	Ba^{2+} ($3d_{5/2}$)
	794.09 ($3d_{3/2}$)	795.15	—	Ba^{2+} ($3d_{3/2}$)
C 1*s*	283.74	284.80	—	Adventitious carbon (C − C/C − H)
	287.90	288.96	$\Delta E_B = +4.16$	Carbonate carbon (O − C = O)
Yb 4*d*	184.30	185.36	$\Delta E_{pk} = 6.64$[a]	Yb^{3+} ($4d^9 4f^{13}$ lower multiplet)
	188.50	189.56	—	Yb^{3+} ($4d^9 4f^{13}$ intermediate multiplet)
	190.95	192.01	—	Yb^{3+} ($4d^9 4f^{13}$ upper multiplet)

[a]Empirical separation between the two main envelope maxima of the Yb^{3+} $4d^9 4f^{13}$ multiplet.

TABLE IV. Comparison of structural motifs and reported Curie–Weiss parameters of $Ba_3Yb_2O_5CO_3$ with representative Yb^{3+} ($4f^{13}$, $\mu_{free} = 4.54\,\mu_B$) oxyanion and oxide magnets. Here μ_{eff}^{HT} and θ_{CW}^{HT} denote high-temperature ($T \gtrsim 150$ K) fit parameters (which are strongly influenced by thermally populated crystal-electric-field levels), whereas μ_{eff}^{LT} and θ_{CW}^{LT} denote low-temperature ($T \lesssim 10$–20 K) parameters probing the lowest Kramers doublet.

Compound	Space Group / Motif	μ_{eff}^{HT} (μ_B)	θ_{CW}^{HT} (K)	μ_{eff}^{LT} (μ_B)	θ_{CW}^{LT} (K)	Low-T State / Ref.
$Ba_3Yb_2O_5CO_3$	$P4/mmm$ (square bilayer)	4.42(3)	−60.8(1.5)	—[a]	—[a]	Paramagnetic to 2 K (This work)
$Yb_2O_2CO_3$	$P6_3/mmc$ (triang. bilayer)	∼ 4.5	—	3.34	−1.36	No LRO to 0.03 K; SRO 0.6 K [25]
$Ba_3Yb(BO_3)_3$	$P6_3cm$ (triang. lattice)	4.59	−95	3.51	−0.07	Paramagnetic to 0.06 K [26]
$NaYbO_2$	$R\bar{3}m$ (triang. layer)	4.54	−65	2.84	−5.6	QSL candidate to 0.05 K [27]
$Yb_2Ti_2O_7$	$Fd\bar{3}m$ (pyrochlore)	4.5	−60	3.1	+0.5–0.8	Orders at $T_C \approx 0.26$ K [44, 45]
Yb_2O_3	$Ia\bar{3}$ (C-type oxide)	4.64	−81	3.67	−9.0	AFM below $T_N = 2.3$ K [28]

[a]Not determined in the present work due to the 2 K base-temperature cutoff, the proximity of the Yb_2O_3 impurity ordering ($T_N = 2.3$ K), and the absence of sub-kelvin susceptibility, low-T high-field $M(H)$, and heat-capacity measurements.

1. *Low-Temperature Permittivity Plateau ($T < 150$ K):* Below 150 K, $\varepsilon'(T)$ exhibits minimal temperature and frequency dependence between 107 Hz and 1 MHz, forming a plateau of $\varepsilon' \approx 40$–45 with $\tan\delta < 10^{-3}$ in both cooling and heating runs. Because thermally activated charge transport is frozen out below 150 K, this plateau reflects the bulk lattice polarizability of the polycrystalline compact; however, because pellet porosity and geometric edge corrections were not independently quantified, $\varepsilon' \approx 40$–45 represents an effective uncorrected ceramic value rather than a porosity-corrected intrinsic permittivity.

2. *High-Temperature Maxwell–Wagner Step and Leakage Regime ($T > 150$ K):* Above 150 K, $\varepsilon'(T)$ rises steeply at low frequencies while $\tan\delta$ increases by several orders of magnitude, reaching $\varepsilon' \approx 430$ and $\tan\delta \approx 62$ at 107 Hz and 300 K during cooling, versus $\varepsilon' \approx 205$ and $\tan\delta \approx 4.8$ during heating. At 1 MHz, where slow interfacial charges cannot follow the AC field, ε' remains near 50–60 up to 300 K.

The large low-frequency permittivity ($\varepsilon' > 200$–400), enormous dissipation factor ($\tan\delta \approx 5$–$60 \gg 1$), and nearly two-fold difference between the cooling and heating sweeps above 200 K are classic signatures of extrinsic Maxwell–Wagner interfacial polarization, DC leakage conductivity, and electrode contact effects in a polycrystalline compact [29–32]. Specifically, applying conductive silver paint to a pellet sintered at 950 °C (which likely retains significant open/closed porosity) creates inhomogeneous sample–electrode contacts and resistive grain boundaries; thermally activated carrier migration and trace moisture adsorption/desorption between the cooling and heating sweeps produce strong history dependence and large apparent low-frequency capacitances without any underlying ferroelectric or structural transition [29, 32].

Because no relaxation peak in $\varepsilon''(f)$ or $\tan\delta(f)$ was resolved within the 107 Hz–1 MHz window (the high-temperature $\tan\delta$ is dominated by the $1/\omega$ conduction tail) and complex impedance/modulus (Z^*/M^*) or Arrhenius analyses could not be reliably extracted from the leakage-dominated data, the present measurements do not test whether the orientationally disordered CO_3^{2-} groups contribute a dipolar relaxation mode. Denser pellets (e.g., prepared via spark plasma sintering or hot pressing with sputtered Au electrodes) and terahertz/infrared spectroscopy would be required to probe bulk carbonate dynamics. Finally, the fact that the extrinsic Maxwell–Wagner onset ($T \approx 150$ K) occurs near the temperature where $1/(\chi - \chi_0)$ departs from the high-temperature Curie–Weiss line is a coincidence between thermally activated grain-boundary conduction

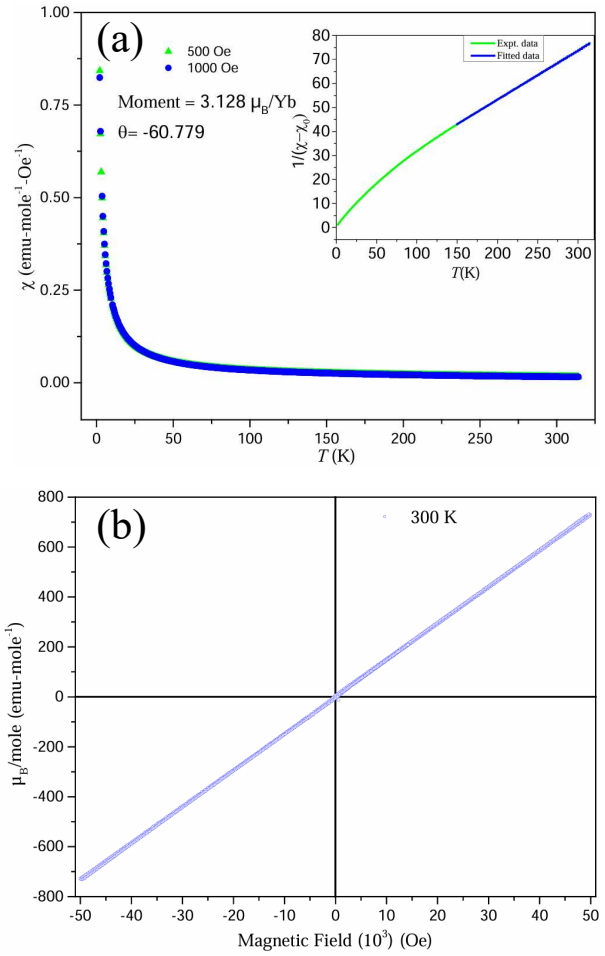


FIG. 4. (a) Temperature dependence of the molar magnetic susceptibility $\chi(T)$ (per mole of $Ba_3Yb_2O_5CO_3$ formula unit) measured at $H = 500$ Oe and 1000 Oe from 2 K to 314 K. The inset plots the inverse temperature-dependent susceptibility $1/(\chi - \chi_0)$ alongside the modified Curie–Weiss fit (blue line) over 150–314 K ($C_{\mathrm{f.u.}} = 4.89(6)$ emu $\cdot$ K $\cdot$ mol$^{-1}_{\mathrm{f.u.}}$, $\theta_{\mathrm{CW}} = -60.8(1.5)$ K), yielding a formula-unit moment $\mu_{\mathrm{eff,f.u.}} = \sqrt{8C_{\mathrm{f.u.}}} = 6.256\,\mu_{\mathrm{B}}$/f.u. and a quadrature per-ion moment $\mu_{\mathrm{eff,Yb}} = \mu_{\mathrm{eff,f.u.}}/\sqrt{2} = 4.42(3)\,\mu_{\mathrm{B}}/\mathrm{Yb}^{3+}$ (note that the in-panel text "Moment = $3.128\,\mu_{\mathrm{B}}$/Yb" represents the arithmetic half $\mu_{\mathrm{eff,f.u.}}/2$ rather than the quadrature value $\mu_{\mathrm{eff,f.u.}}/\sqrt{2}$). (b) Isothermal magnetization $M(H)$ recorded at $T = 300$ K up to ± 50 kOe (± 5 T), showing a linear paramagnetic response.

and single-ion Yb^{3+} CEF depopulation, with no evidence for magnetodielectric coupling [31].

IV. CONCLUSION

We have reported room-temperature XPS, DC magnetic susceptibility (2–314 K), and temperature-dependent dielectric permittivity (15–300 K) measurements on the layered perovskite oxycarbonate $Ba_3Yb_2O_5CO_3$, whose synthesis and tetragonal $P4/mmm$ crystal structure were previously established by Deakin *et al.* [21]. Room-temperature powder XRD confirms the $P4/mmm$ unit cell ($a = 4.326(1)$ Å, $c = 11.915(3)$ Å), while comparison with the published neutron structure ($a = 4.3258(2)$ Å, $c = 11.9036(5)$ Å) [21] highlights the necessity of neutron diffraction for locating the light C and O sites in the presence of heavy Ba and Yb scatterers.

Core-level XPS resolves two O 1s ($\Delta E_B = +0.81$ eV) and C 1s ($\Delta E_B = +4.16$ eV) components alongside a Yb 4d ($4d^9 4f^{13}$) multiplet profile consistent with trivalent Yb^{3+} and an insulating valence-band edge ~ 2.5–3.0 eV below E_F, though surface $BaCO_3$ formation on air-exposed barium oxides prevents an unambiguous separation of surface and bulk carbonate signals by unetched XPS alone. DC magnetic susceptibility shows paramagnetic behavior down to 2 K without long-range order. A three-parameter modified Curie–Weiss fit over 150–314 K recovers $\mu_{\mathrm{eff,Yb}} = 4.42(3)\,\mu_{\mathrm{B}}/\mathrm{Yb}^{3+}$ (near the $4.54\,\mu_{\mathrm{B}}$ free-ion value) and $\theta_{\mathrm{CW}} = -60.8(1.5)$ K, where comparison with related Yb^{3+} oxides and oxycarbonates demonstrates that θ_{CW} and the low-temperature curvature below 150 K are governed by CEF splitting of the $^2F_{7/2}$ manifold and parameter covariance with χ_0 rather than large inter-site exchange. Dielectric scans on silver-painted pellets show a weakly temperature-dependent plateau ($\varepsilon' \approx 40$–45, $\tan\delta < 10^{-3}$, uncorrected for porosity) below 150 K and an extrinsic Maxwell–Wagner and leakage-dominated rise above 150 K. Future studies employing FTIR/TGA-MS, dense pellets with sputtered contacts, and sub-kelvin magnetization and heat-capacity measurements will be essential to characterize the $J_{\mathrm{eff}} = 1/2$ ground state and intrinsic bulk dielectric response of $Ba_3Yb_2O_5CO_3$.

ACKNOWLEDGMENTS

The authors gratefully acknowledge the Saha Institute of Nuclear Physics (SINP), Kolkata for institutional support and access to experimental and central measurement facilities.

CONFLICTS OF INTEREST

There are no conflicts of interest to declare.

DATA AVAILABILITY STATEMENT

The datasets supporting the findings of this study are available from the corresponding author upon reasonable request.

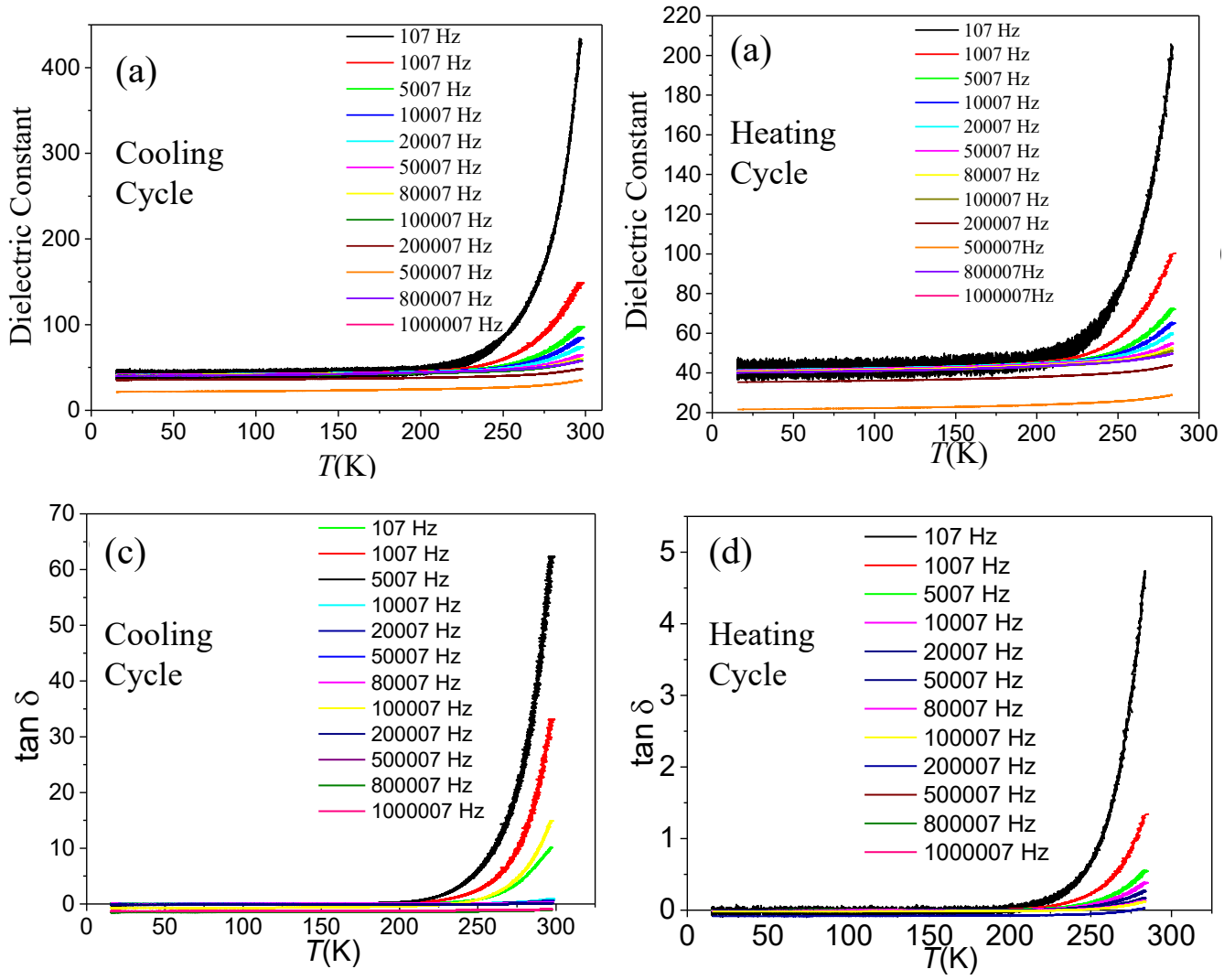


FIG. 5. Temperature-dependent dielectric response of a sintered polycrystalline pellet of $Ba_3Yb_2O_5CO_3$ measured between 15 K and 300 K at frequencies from 107 Hz to 1 000 007 Hz ($\sim$ 1 MHz): (a) real part of the permittivity (ε', cooling cycle; top-left panel); (b) ε' during the heating cycle (top-right panel, labeled "(a) Heating Cycle" in the raw plot); (c) dielectric loss tangent ($\tan\delta$, cooling cycle; bottom-left panel); and (d) $\tan\delta$ during the heating cycle (bottom-right panel).

[1] Daniel I. Khomskii. *Transition Metal Compounds*. Cambridge University Press, Cambridge, 2014.

[2] J. M. D. Coey. *Magnetism and Magnetic Materials*. Cambridge University Press, Cambridge, 2010.

[3] Richard J. D. Tilley. *Perovskites: Structure–Property Relationships*. John Wiley & Sons, Chichester, 2016.

[4] J. Paul Attfield. Principles and applications of structure–property relationships in perovskites. *APL Mater.*, 3(4):041510, 2015.

[5] G. Catalan and J. F. Scott. Physics and applications of bismuth ferrite. *Adv. Mater.*, 21(24):2463–2485, 2009.

[6] John B. Goodenough. Theory of the role of covalence in the perovskite-type manganites [La, Ca]MnO_3. *Phys. Rev.*, 100(2):564–573, 1955.

[7] Peter R. Slater. Oxyanion incorporation into perovskite-related materials. *J. Mater. Chem.*, 16(38):3793–3802, 2006.

[8] Colin Greaves. Oxyanion-containing perovskite-related phases. *Curr. Opin. Solid State Mater. Sci.*, 12(5–6):90–97, 2008.

[9] Cédric Tassel and Hiroshi Kageyama. Mixed-anion compounds: a new horizon in solid-state chemistry. *Chem. Soc. Rev.*, 45(14):4064–4076, 2016.

[10] Hiroshi Kageyama, Katsuro Hayashi, Kazuhiko Maeda, J. Paul Attfield, Zenji Hiroi, James M. Rondinelli, and Kenneth R. Poeppelmeier. Expanding frontiers in ma-

terials chemistry and physics with multiple anions. *Nat. Commun.*, 9(1):772, 2018.

[11] Tripurari Sharan Tripathi and Maarit Karppinen. Mixed-anion compounds: An unexplored playground for ALD fabrication. *Adv. Mater. Interfaces*, 8(11):2100146, 2021.

[12] Yange Luan, Yumin Li, Zhong Li, Bao Yue Zhang, and Jian Zhen Ou. Layered anion-mixed oxycompounds: Synthesis, properties, and applications. *Adv. Sci.*, 12(12):2500477, 2025.

[13] Teruki Motohashi, Maarit Karppinen, Simon J. Clarke, and Hiroshi Kageyama. Mixed-anion compounds. *Dalton Trans.*, 54(41):15361–15363, 2025.

[14] T. Chakraborty, T. Saha-Dasgupta, Sugata Ray, and S. Majumdar. Anomalous magnetic and dielectric response in $Ba_5Co_5ClO_{13}$. *Phys. Rev. B*, 90(23):235147, 2014.

[15] J. Atanelov and Peter Mohn. Magnetic properties of carbon substituted $GaFeO_3$: An *ab initio* study. *Comput. Mater. Sci.*, 117:380–389, 2016.

[16] Qing-Yu Xu, Wen Zheng, and J.-M. Liu. Enhanced polarization and ferromagnetism in N-doped $BiFeO_3$. *Phys. Rev. B*, 84(9):094438, 2011.

[17] Y. C. Hu and Z. Z. Jiang. Fluorine substitution effects on structural and multiferroic properties of $BiFeO_3$. *Phys. Lett. A*, 376(4):62–66, 2012.

[18] Bernard Raveau, C. Michel, Maryvonne Hervieu, and D. Groult. *Crystal Chemistry of High-T_c Superconducting Copper Oxides*. Springer-Verlag, Berlin, Heidelberg, 1991.

[19] A. Robert Armstrong and Peter P. Edwards. Synthesis and structural characterization of the oxycarbonate $Sr_2CuO_2(CO_3)$. *J. Solid State Chem.*, 103(2):312–320, 1993.

[20] K. Kinoshita and T. Yamada. A new copper-oxide superconductor containing carbon: $(Ba,Sr)_4Cu_2(CO_3)O_{4+\delta}$. *Nature*, 357:313–315, 1992.

[21] Joshua Deakin, Ivan Trussov, Alexandra S. Gibbs, Emma Kendrick, and Peter R. Slater. Carbonate: an alternative dopant to stabilize new perovskite phases; synthesis and structure of $Ba_3Yb_2O_5CO_3$ and related isostructural phases $Ba_3Ln_2O_5CO_3$ (Ln = Y, Dy, Ho, Er, Tm and Lu). *Dalton Trans.*, 47(37):12901–12906, 2018.

[22] T. N. Khamaganova, N. M. Kuperman, and Z. G. Bazarova. Synthesis and crystal structure of $Ba_3Ln_4O_9$ (Ln = Yb, Lu). *J. Solid State Chem.*, 145(1):33–36, 1999.

[23] L. M. Lopato, I. M. Maister, and A. V. Shevchenko. Phase equilibria in the system BaO–Yb_2O_3. *Inorg. Mater.*, 19:652–655, 1983.

[24] R. D. Shannon. Revised effective ionic radii and systematic studies of interatomic distances in halides and chalcogenides. *Acta Crystallogr. Sect. A*, 32(5):751–767, 1976.

[25] Aya Rutherford, Chengkun Xing, Qing Huang, Eun Sang Choi, Stuart Calder, and Haidong Zhou. Magnetic properties of $R_2O_2CO_3$ (R = Pr, Nd, Gd, Tb, Dy, Ho, Er, Yb) with a rare earth-bilayer of triangular lattice. *Phys. Rev. Mater.*, 8(11):114413, 2024.

[26] Rabindranath Bag, Matthew Ennis, Chunxiao Liu, Sachith E. Dissanayake, Zhenzhong Shi, Jinyu Liu, Leon Balents, and Sara Haravifard. Realization of quantum dipoles in triangular lattice crystal $Ba_3Yb(BO_3)_3$. *Phys. Rev. B*, 104(22):L220403, 2021.

[27] Mitchell M. Bordelon, Eric Kenney, Chunxiao Liu, Tom Hogan, Lorenzo Posthuma, Marzieh Kavand, Yuanqi Lyu, Mark Sherwin, C. R. Dela Cruz, Matthias B. Stone, Leon Balents, Michael J. Graf, and Stephen D. Wilson. Field-tunable quantum disordered ground state in the triangular-lattice antiferromagnet $NaYbO_2$. *Nat. Phys.*, 15(10):1058–1064, 2019.

[28] Sam Mugiraneza and Alannah M. Hallas. Tutorial: a beginner's guide to interpreting magnetic susceptibility data with the Curie–Weiss law. *Commun. Phys.*, 5(1):95, 2022.

[29] P. Lunkenheimer, V. Bobnar, J. Schneider, and A. Loidl. Colossal dielectric constants in single-crystalline and ceramic $CaCu_3Ti_4O_{12}$. *Phys. Rev. B*, 66(5):052105, 2002.

[30] M. A. Subramanian, Dong Li, N. Duan, B. A. Reisner, and A. W. Sleight. High dielectric constant in $ACu_3Ti_4O_{12}$ and $ACu_3Ru_4O_{12}$ phases. *J. Solid State Chem.*, 151(2):323–325, 2000.

[31] G. Catalan. Magnetocapacitance without magnetoelectricity. *Appl. Phys. Lett.*, 88(10):102902, 2006.

[32] Derek C. Sinclair, Timothy B. Adams, Finlay D. Morrison, and Anthony R. West. $CaCu_3Ti_4O_{12}$: One-step internal barrier layer capacitor. *Appl. Phys. Lett.*, 80(12):2153–2155, 2002.

[33] Juan Rodríguez-Carvajal. Recent advances in magnetic structure determination by neutron powder diffraction. *Physica B: Condens. Matter*, 192(1–2):55–69, 1993.

[34] Koichi Momma and Fujio Izumi. VESTA 3 for three-dimensional visualization of crystal, volumetric and morphology data. *J. Appl. Crystallogr.*, 44(6):1272–1276, 2011.

[35] Kolibrik.net. KolXPD: Software for x-ray photoelectron spectroscopy data processing and peak fitting. http://www.kolibrik.net/kolxpd, 2018.

[36] Grzegorz Greczynski and Lars Hultman. X-ray photoelectron spectroscopy: Towards reliable binding energy referencing. *Prog. Mater. Sci.*, 107:100591, 2020.

[37] Grzegorz Greczynski and Lars Hultman. Binding energy referencing in x-ray photoelectron spectroscopy: Expanded data set confirms that adventitious carbon aligns to the sample vacuum level. *Appl. Surf. Sci.*, 670:160666, 2024.

[38] International Centre for Diffraction Data. Powder diffraction file card no. 01-071-6423 ($BaCO_3$, witherite), 2001.

[39] Peter J. Schmitz. Barium oxide (BaO) and barium carbonate ($BaCO_3$) by XPS. *Surf. Sci. Spectra*, 8(3):190–199, 2001.

[40] Paul S. Bagus, Eugene S. Ilton, and Connie J. Nelin. The interpretation of XPS spectra: Insights into materials properties. *Surf. Sci. Rep.*, 68(2):273–304, 2013.

[41] Paul S. Bagus, Connie J. Nelin, and Eugene S. Ilton. Multiplet splitting for the XPS of heavy elements: Dependence on oxidation state. *J. Electron Spectrosc. Relat. Phenom.*, 200:174–185, 2015.

[42] R. J. Iwanowski and J. W. Sobczak. XPS study of Yb and Yb_2O_3. *Acta Phys. Pol. A*, 91(4):807–812, 1997.

[43] Kwang-Won Park and Sungwoo Ahn. Electronic structure and chemical bonding of ytterbium oxide thin films. *Appl. Surf. Sci.*, 364:573–578, 2016.

[44] J. A. Hodges, P. Bonville, A. Forget, M. Rams, K. Królas, and G. Dhalenne. The crystal field in the Yb^{3+} pyrochlore $Yb_2Ti_2O_7$. *J. Phys.: Condens. Matter*, 13(41):9301–9310, 2001.

[45] Jeffrey G. Rau and Michel J. P. Gingras. Frustrated quantum rare-earth pyrochlores. *Annu. Rev. Condens. Matter Phys.*, 10:357–386, 2019.

[46] B. Z. Malkin, A. R. Zakirov, M. N. Kasatkina, M. V. Zverev, and M. N. Popova. Crystal field and magnetic properties of Yb^{3+} ions in rare-earth titanates. *Phys. Solid State*, 46:1448–1456, 2004.

[47] S. Das, S. Kundu, and Sugata Ray. Crystal field splitting and magnetic ground state of trivalent ytterbium in distorted octahedral environments. *Phys. Rev. B*, 104(12):125110, 2021.

[48] Andrew T. Boothroyd. *Principles of Neutron Scattering from Condensed Matter*. Oxford University Press, Oxford, 2020.

[49] Anatole Abragam and Brebis Bleaney. *Electron Paramagnetic Resonance of Transition Ions*. Oxford University Press, Oxford, 2012.

[50] Junjiro Kanamori. Superexchange interaction and symmetry properties of electron orbitals. *J. Phys. Chem. Solids*, 10(2–3):87–98, 1959.